Research Article

High-entropy perovskite RETa$_3$O$_9$ ceramics for high-temperature environmental/thermal barrier coatings

Lin CHEN, Baihui LI, Jun GUO, Yuke ZHU, Jing FENG[*]

*Faculty of Material Science and Engineering, Kunming University of
Science and Technology, Kunming 650093, China*

Abstract: Four high-entropy perovskite (HEP) RETa$_3$O$_9$ samples were fabricated via a spark plasma sintering (SPS) method, and the corresponding thermophysical properties and underlying mechanisms were investigated for environmental/thermal barrier coating (E/TBC) applications. The prepared samples maintained low thermal conductivity (1.50 W·m^{-1}·K^{-1}), high hardness (10 GPa), and an appropriate Young's modulus (180 GPa), while the fracture toughness increased to 2.5 MPa·m$^{1/2}$. Nanoindentation results showed the HEP ceramics had excellent mechanical properties and good component homogeneity. We analysed the influence of different parameters (the disorder parameters of the electronegativity, ionic radius, and atomic mass, as well as the tolerance factor) of A-site atoms on the thermal conductivity. Enhanced thermal expansion coefficients, combined with a high melting point and extraordinary phase stability, expanded the applications of the HEP RETa$_3$O$_9$. The results of this study had motivated a follow-up study on tantalate high-entropy ceramics with desirable properties.

Keywords: high-entropy ceramics (HECs); tantalates; thermal conductivity; nanoindentation; fracture toughness

1　Introduction

Oxide environmental/thermal barrier coatings (E/TBCs) have been extensively investigated to increase the working temperatures of aircraft engines, gas turbines, and hypersonic vehicles [1–6]. E/TBCs are applied to ceramic/alloy substrates to decrease surface temperatures and prevent damage from high-speed impact particles, molten oxides, and other environmental factors [2–12]. Rare earth (RE) tantalates (RETaO$_4$, RE$_3$TaO$_7$, and RETa$_3$O$_9$) are considered novel E/TBCs because of extraordinary thermophysical properties [4,8,13–15]. It

has been reported that tantalates have low thermal conductivity and high hardness, melting points, and thermal expansion coefficients. However, tantalates also have clear shortcomings, e.g., RETa$_3$O$_9$ has inadequate fracture toughness (1.1–1.5 MPa·m$^{1/2}$) [15]. Diverse methods are used to enhance the properties of RETaO$_4$ [8,13] and RE$_3$TaO$_7$ ceramics [14,16], and our aim is to stimulate the investigation and application of RETa$_3$O$_9$ with perovskite structures. Some scholars have identified perovskite oxides as promising E/TBCs, and high-entropy ceramics (HECs) are being studied in various fields [15,17–19]. Wright *et al.* [20] have reported that HECs of RE$_2$Zr$_2$O$_7$ exhibit low thermal conductivity and high stiffness, and Liu *et al.* [17] have proven that the thermal properties of perovskite-type

---

* Corresponding author.
E-mail: jingfeng@kust.edu.cn

(ABO_3) ceramics can be regulated by entropy engineering. Furthermore, HECs of $RE_2Si_2O_7$, RE_3NbO_7, and other RE tantalates have been studied for use as E/TBCs [21–24]. One of the most striking features of HECs is that multifarious properties can be successfully tailored to meet the demands of specific applications.

The structure of HECs is similar to that of high-entropy alloys (HEAs), that is, one or more Wyckoff sites in lattices are occupied by identical or near-identical atoms. In HECs, more than four types of atoms occupy one site, and the configurational entropy is higher than $1.5R$ (where R denotes the gas constant); the configurational entropy (ΔS_{conf}) is expressed as $\Delta S_{conf} = R \times \ln N$, where N is the number of elements in one sublattice [5,25–27]. The configurational entropy increases with the number of types of atoms in one or more Wyckoff sites in the lattice. Herein, we regulate the configurational entropy by controlling the types of atoms in the lattice. Theoretically, the highest configurational entropy is obtained for some materials when all the elements in a sublattice have the same atomic fraction [28,29]. To date, HECs have been fabricated with many excellent properties, including enhanced hardness and toughness [19], regulation of thermal transportation properties [20,23], increased corrosion resistance [21], and strengthened high-temperature phase stability [10,17]. HECs of RE_3TaO_7 [16], $RE_2Zr_2O_7$ [20,23], RE_3NbO_7 [22], and $RE_3Al_5O_{12}$ [30] have also been investigated for use as TBCs, whereas HECs of $RE_2Si_2O_7$ [21] and RE_2SiO_5 [31] have been investigated for use as EBCs. Currently, multifunctional thermal and environmental barrier integration coatings are used to improve the high-temperature performance of components of alloys and ceramic matrix composites. A few oxides meet the requirements of multifunctional E/TBCs. Perovskite-type ceramics typically have high melting points [17], low thermal conductivity [15,17,18], regulatable mechanical properties [17,32,33], etc. [34,35]. Accordingly, multifarious perovskite-type oxides have been fabricated to improve the properties and expand the applications [15,17,18,33–36]. In this study, we optimize the properties of HECs of $RETa_3O_9$ ($RE_{0.33}TaO_3$) perovskites as high-temperature E/TBCs. Differences in ionic radii and atomic weights of constituent elements affect the crystal structures and thermophysical properties of HECs. Therefore, a two-step sintering process is used to prepare four different equiatomic high-entropy perovskite (HEP) tantalates, including $(La_{1/5}Pr_{1/5}Dy_{1/5}Ho_{1/5}Tm_{1/5})Ta_3O_9$ (5HEP-1), $(Gd_{1/5}Dy_{1/5}Ho_{1/5}Er_{1/5}Tm_{1/5})Ta_3O_9$ (5HEP-2), $(La_{1/6}Sm_{1/6}Eu_{1/6}Dy_{1/6}Ho_{1/6}Tm_{1/6})Ta_3O_9$ (6HEP-3), and $(Eu_{1/6}Gd_{1/6}Dy_{1/6}Ho_{1/6}Er_{1/6}Tm_{1/6})Ta_3O_9$ (6HEP-4). The ionic radii and atomic weights of La and Pr are considerably different from those of Dy, Ho, and Tm in 5HEP-1, whereas Gd, Dy, Ho, Er, and Tm in 5HEP-2 have similar ionic radii and atomic weights. That is, differences in the ionic radius and atomic weight among the RE elements in 5HEP-1 are more prominent than those in the 5HEP-2 sample. The aforementioned designs are reproduced in the 6HEP-3 and 6HEP-4 samples to investigate the impacts of differences in ionic radii and atomic weights of various RE elements.

2 Experimental

2. 1 Material fabrication

HEP $RETa_3O_9$ powders were synthesized by a high-temperature sintering process without pressure. We used RE_2O_3 (RE = La, Sm, Eu, Gd, Dy, Ho, Er, Tm), Pr_6O_{11}, and Ta_2O_5 with 99.9% purity as raw powders, which had particle sizes less than 10 μm. The weighed powders were mixed by a ball mill (300 r·min^{-1}, 12 h) using alcohol as the dispersion medium, and then placed in a drier at 90 ℃ for 6 h to evaporate alcohol. The dried powders were maintained at 1600 ℃ for 10 h to obtain high-purity $RETa_3O_9$ powders. The prepared powders were passed through a 500-mesh sieve, and approximately 2.5 g of the sieved powders were sintered by spark plasma sintering (SPS). The final SPS parameters were 1600 ℃, 100 MPa, 10-min sintering time, and a heating rate of 50 ℃·min^{-1}. For comparison, a dense yttria-stabilized zirconia (YSZ) bulk ceramic was synthesized and tested using the same methods.

2. 2 Structure identification

The X-ray diffractometer (MiniFlex 600, Rigaku, Japan) was applied to confirm the crystal structures and lattice constants of the HEP $RETa_3O_9$. The X-ray diffraction (XRD) 2θ angle was ranged between 20° and 60°, and the scanning speed was 5 (°)·min^{-1}. The exact lattice constants, unit cell volumes, and theoretical densities of each sample were computed from the XRD patterns. The scanning electronic microscope (SEM, JSM-7800F, JEOL, Japan) and the energy-dispersive spectroscope (EDS, 6751A-6UUS-SN, Thermo Scientific, USA)

were used to probe the surface structures. We used SEM and EDS to observe the grain sizes, pores, cracks, and elemental distributions.

2. 3 Mechanical property testing

The hardness (H) and fracture toughness (K_{IC}) were determined by the lengths of indentation diagonal (d) and the indentation crack (c) using a hardness tester (DHV-1000Z-CCD, SZNG, China). Each sample was tested 10 times, the minimum and maximum results were removed, and the remaining results were used to calculate the average values. The fracture toughness increased with the surface fracture energy (Γ), and was calculated as below [37,38]:

$$H = 0.464 \frac{F}{d^2} \tag{1}$$

$$K_{IC} = 0.018 \sqrt{\frac{E}{H}} \cdot \frac{F}{c^{1.5}} \tag{2}$$

$$\Gamma = \frac{2\zeta^2 F d^2}{c^3} \tag{3}$$

where $F = 4.9$ N, $\zeta = 0.016$, and E denotes the Young's modulus measured using the ultrasonic equipment (UMS-100, TECLAB, France) [39]:

$$E = \frac{\rho V_t^2 (3V_l^2 - 4V_t^2)}{V_l^2 - V_t^2} \tag{4}$$

where ρ is the sample density, and V_l and V_t are the longitudinal and transverse acoustic velocities, respectively.

To eliminate the effect of the microstructure on the mechanical properties, the nano-Young's modulus (E_N) and nano-hardness (H_N) were simultaneously measured using the nanoindentation device (iNano instrument, iMicro, USA). During the nanoindentation test, we applied both E and H mapping (three-dimensional (3D) mapping) and advanced dynamic E and H (single-point test) models, where the highest test load was 100 mN. A total of $30 \times 30 = 900$ points were tested over a 300 μm × 300 μm area at intervals of 10 μm during the 3D mapping measurement. The advanced dynamic E and H tests were used to determine how the hardness and Young's modulus varied with the indentation load and depth, and the results were analysed.

2. 4 Thermal property testing

The thermal expansion coefficients (TECs) were calculated based on the elongation caused by increasing the temperature that was measured by a thermo-

mechanical analysis device (TMA 402 F3, NETZSCH, Germany). The thermal diffusivity (λ, 25–900 ℃) was measured using the laser reflection device (LFA 457, NETZSCH, Germany), and the thermal conductivity (k) was calculated from λ, density (ρ), porosity (ϕ), and heat capacity (C_p) as follows [40]:

$$k = \frac{\lambda \cdot \rho \cdot C_p}{1 - 4\phi / 3} \tag{5}$$

The phonon mean free path (l) was calculated using the relationship between the thermal diffusivity (λ) and the mean acoustic velocity (V_m) [40–42]:

$$l = \frac{3\lambda}{V_m} \tag{6}$$

The mean acoustic velocity (V_m) was calculated from V_l and V_t [39]:

$$V_m = \left[\frac{1}{3} \left(\frac{1}{V_l^3} + \frac{2}{V_t^3} \right) \right]^{-\frac{1}{3}} \tag{7}$$

3 Results and discussion

3. 1 Crystal structures

Figure 1(a) shows that the main XRD peaks of the four HEP RETa$_3$O$_9$ samples coincide with PDF#52-0567 with the $P4/mmm$ space group. A RETaO$_4$ precipitate (PDF#24-0379) is detected in 5HPE-2, 6HEP-3, and 6HEP-4, whereas the minor peaks at 2θ angles of 25°–30° for 5HEP-1 are associated with a different RETaO$_4$ phase (PDF#19-1013). The weak peaks of RETaO$_4$ indicate that the RETaO$_4$ content is too low to dominate the thermophysical properties of the prepared samples. In Ref. [43], the crystalline temperature of YTaO$_4$ is reported to be approximately 840 ℃, and this low crystalline temperature may be the cause of the RETaO$_4$ precipitate in the prepared HEP samples. The lattice of RETa$_3$O$_9$ (RE$_{1/3}$TaO$_3$) with the $P4/mmm$ space group is treated as a defect perovskite (A$_{1/3}$BO$_3$-type) structure when a 1/3 vacancy is created in the RE cationic sublattice, as shown in Fig. 1(b). Each Ta is surrounded by six oxygens to form a [TaO$_6$] octahedron, and the octahedra are connected to each other at the corners. These octahedrons are twisted structures, because the Ta–O bond lengths vary. The distortion degree of perovskites depends on the octahedral twist. Normally, the tolerance factor (t) is an indicator of the
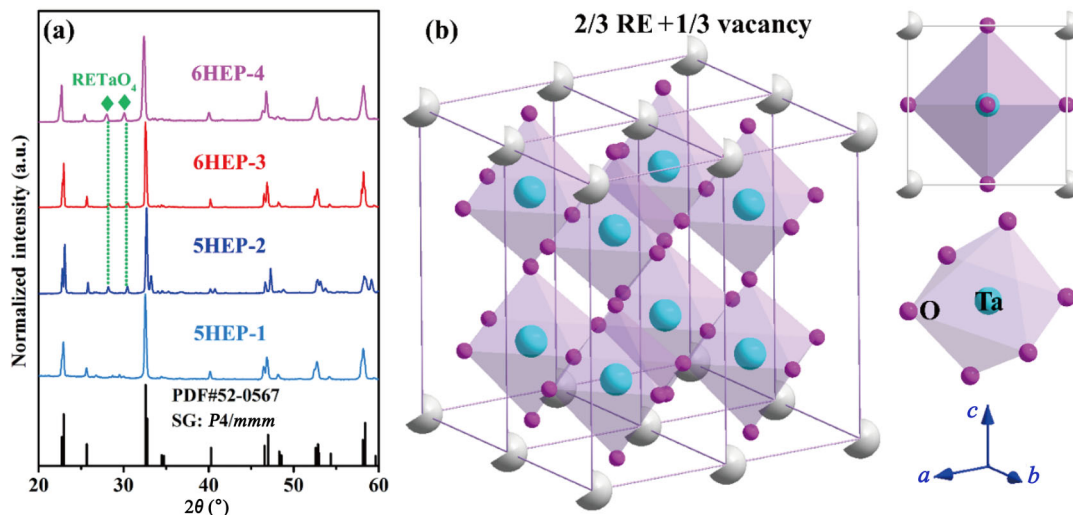
Fig. 1 Characterization of the crystal structure of $(La_{1/5}Pr_{1/5}Dy_{1/5}Ho_{1/5}Tm_{1/5})Ta_3O_9$ (5HEP-1), $(Gd_{1/5}Dy_{1/5}Ho_{1/5}Er_{1/5}Tm_{1/5})Ta_3O_9$ (5HEP-2), $(La_{1/6}Sm_{1/6}Eu_{1/6}Dy_{1/6}Ho_{1/6}Tm_{1/6})Ta_3O_9$ (6HEP-3), and $(Eu_{1/6}Gd_{1/6}Dy_{1/6}Ho_{1/6}Er_{1/6}Tm_{1/6})Ta_3O_9$ (6HEP-4): (a) normalized XRD patterns; (b) $2 \times 2 \times 1$ unit cell, where the grey ball represents an A-site 2/3 RE atom with a 1/3 vacancy, the blue ball represents a B-site Ta atom, and the purple ball represents an oxygen atom.

Table 1 Design composition, sample name, lattice parameters (*a*, *b*, and *c*), unit cell volume (*V*), theoretical density (ρ_0), and porosity (ϕ) of HEP RETa$_3$O$_9$ ceramics

Composition	Sample	a (Å)	b (Å)	c (Å)	V (Å^3)	ρ_0 (g·cm^{-3})	ϕ (%)
$(La_{1/5}Pr_{1/5}Dy_{1/5}Ho_{1/5}Tm_{1/5})Ta_3O_9$	5HEP-1	3.878	3.878	7.850	118.081	7.89	1.5
$(Gd_{1/5}Dy_{1/5}Ho_{1/5}Er_{1/5}Tm_{1/5})Ta_3O_9$	5HEP-2	3.854	3.854	7.864	116.796	8.06	1.3
$(La_{1/6}Sm_{1/6}Eu_{1/6}Dy_{1/6}Ho_{1/6}Tm_{1/6})Ta_3O_9$	6HEP-3	3.902	3.902	7.803	118.834	7.86	2.0
$(Eu_{1/6}Gd_{1/6}Dy_{1/6}Ho_{1/6}Er_{1/6}Tm_{1/6})Ta_3O_9$	6HEP-4	3.854	3.854	7.837	116.396	8.07	2.2

lattice stability and distortion degree of perovskite structures [29,32]:

$$t = \frac{r_A + r_O}{\sqrt{2}\,(r_{Ta} + r_O)} \tag{8}$$

where r_A, r_O, and r_{Ta} are the effective ionic radii of RE^{3+}, O^{2-}, and Ta^{5+} ions, respectively. Perovskite oxides have a stable lattice when t ranges from 0.8 to 1, and they may crystallize into an orthorhombic phase for t less than 0.9 [29,32]. The tolerance factors of the HEP RETa$_3$O$_9$ are proportional to the A-site ionic sizes, and are 0.871, 0.855, 0.866, and 0.856 for 5HEP-1, 5HEP-2, 6HEP-3, and 6HEP-4, respectively. Among the four prepared samples, 5HEP-2 has the maximum lattice distortion degree based on the minimum tolerance factor. The results presented in Table 1 and Fig. 1(b) indicate that the length of the *c*-axis is almost twice that of the *a*- and *b*-axes, because HEP RETa$_3$O$_9$ is an orthorhombic phase. Usually, the lengths of the *a*-, *b*-, and *c*-axes of ABO$_3$-type perovskites are almost equal (corresponding to a cubic phase), and the

structures of the HEP RETa$_3$O$_9$ are also called double-perovskite structures [18]. Herein, the $2 \times 2 \times 1$ unit cell of HEP RETa$_3$O$_9$ is similar to that of cubic ABO$_3$ perovskites.

3.2 Microstructures

The four HEP bulk samples are polished using diamond sandpapers, and then held at 1400 ℃ for 3 h to observe the surface grains and elemental distributions by SEM and EDS. In Fig. 2, most grains are smaller than 5 μm, and the RE elements are homogeneously distributed in the prepared samples. The prepared HEP samples have smaller grains than the single-rare-earth RETa$_3$O$_9$, and grain refinement is achieved in the HEP RETa$_3$O$_9$ samples [15]. The mean grain sizes are 5–7 μm for the single-rare-earth RETa$_3$O$_9$ ceramics and less than 2 μm for the HEP samples. Thus, the corresponding reduction in the grain size is higher than 50%, and we investigate the effect of this reduction on the material properties. Some nanoscale grains are found in 5HEP-2, 6HEP-3, and 6HEP-4, and it is inferred that these grains
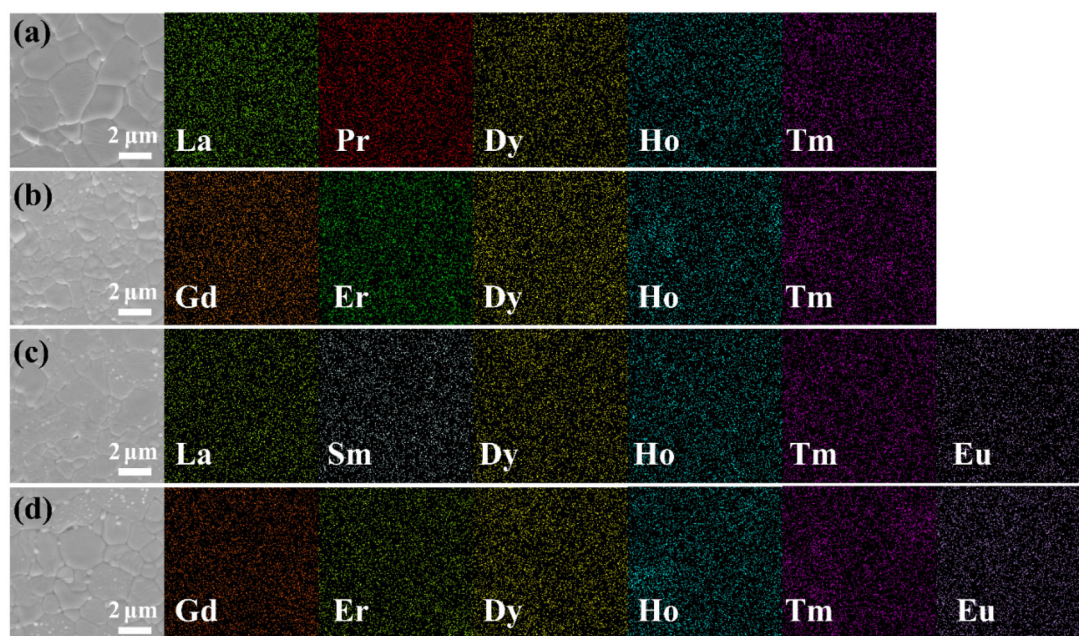
Fig. 2 Surface grains and RE elemental distributions of HEP RETa$_3$O$_9$ ceramics: (a) (La$_{1/5}$Pr$_{1/5}$Dy$_{1/5}$Ho$_{1/5}$Tm$_{1/5}$)Ta$_3$O$_9$ (5HEP-1), (b) (Gd$_{1/5}$Dy$_{1/5}$Ho$_{1/5}$Er$_{1/5}$Tm$_{1/5}$)Ta$_3$O$_9$ (5HEP-2), (c) (La$_{1/6}$Sm$_{1/6}$Eu$_{1/6}$Dy$_{1/6}$Ho$_{1/6}$Tm$_{1/6}$)Ta$_3$O$_9$ (6HEP-3), and (d) (Eu$_{1/6}$Gd$_{1/6}$Dy$_{1/6}$Ho$_{1/6}$Er$_{1/6}$Tm$_{1/6}$)Ta$_3$O$_9$ (6HEP-4).

constitute the RETaO$_4$ precipitate. We used the backscattered electron (BSE) model to analyse the grains, and no difference was found between nano- and micron-scale grains. The RETaO$_4$ and RETa$_3$O$_9$ phases are comprised of the same elements, and the grains of these phases have the same atomic contrast. Furthermore, the EDS results show no elemental segregation. The XRD, SEM, and EDS analyses imply that we can neglect the influence of RETaO$_4$ on the properties of the prepared samples. In Table 1, the porosities of the prepared samples are 1%–3%, which are lower than those of the samples synthesized via a solid-state reaction [15]. Hence, dense and high-purity HEP RETa$_3$O$_9$ ceramics can be fabricated via an SPS process. The grain size, grain boundary density, cracks, and pores affect the properties of structural ceramics, as discussed in the following sections.

3.3 Mechanical properties

As shown in Table 2, the HEP RETa$_3$O$_9$ ceramics have a Young's modulus (E), hardness (H), and toughness (K_{IC}) of 130–180 GPa, 7–10 GPa, and 1.8–2.5 MPa·m$^{1/2}$, respectively. YSZ has a high Young's modulus (220–250 GPa), which results in inadequate deformation tolerance [44]. For comparison, a YSZ bulk sample is fabricated and tested using the aforementioned methods. A balance among different

mechanical properties is achieved in the HEP RETa$_3$O$_9$. Figure 3 shows that the four HEP samples have a lower Young's modulus than those of YSZ and La$_2$Zr$_2$O$_7$ (230 GPa) [6], and 6HEP-4 has the highest toughness (2.5±0.4 MPa·m$^{1/2}$). The HEP ceramics and single-rare-earth RETa$_3$O$_9$ have similar Young's moduli (140–200 GPa) and hardness (7.0–10.0 GPa), whereas the toughness of the HEP RETa$_3$O$_9$ is 1.8–2.5 MPa·m$^{1/2}$. Figures 4(a)–4(c) show that the hardness–Young's modulus, toughness–Young's modulus, and toughness–hardness curves are not linear. The results presented in Fig. 4(d) and Table 2 indicate that the toughness is proportional to the surface fracture energy. Equation (3) shows that the surface fracture energy is related to the lengths of indentation and cracks, and is an intrinsic feature of these materials. To study the ductile and brittle features of the four samples, we calculate the G/B ratio, where G and B represent the shear and bulk moduli, respectively [39,45]:

$$B = \frac{E}{3(1-2v)} \tag{9}$$

$$G = \frac{E}{2(1+v)} \tag{10}$$

where v is the Poisson's ratio, as measured by ultrasonic equipment. Materials with a G/B ratio less than 0.57 are brittle, and materials with a G/B ratio higher than

Table 2 Young's modulus and nano-Young's modulus (E and E_N), hardness and nano-hardness (H and H_N), fracture toughness (K_{IC}), mean acoustic velocity (V_m), surface fracture energy ($\varGamma$), and G/B ratio of HEP RETa$_3$O$_9$ ceramics

Sample	E_N (GPa)	H_N (GPa)	V_m (m·s^{-1})	E (GPa)	H (GPa)	K_{IC} (MPa·m$^{1/2}$)	$\varGamma$ (J·m^{-2})	G/B
5HEP-1	178.9±8.7	10.8±0.6	3270.5±17.3	172.5±11.5	9.0±0.3	1.8±0.4	19.1±7.2	0.55
5HEP-2	143.3±12.7	10.0±1.3	2945.5±5.4	139.2±8.6	7.3±1.3	2.0±0.3	27.2±8.5	0.59
6HEP-3	156.7±5.3	10.4±0.6	3214.1±10.6	157.8±10.9	9.1±0.3	2.1±0.3	25.6±7.8	0.62
6HEP-4	180.5±13.6	10.6±1.1	3215.3±28.1	178.2±8.2	9.0±0.4	2.5±0.4	32.7±10.0	0.61
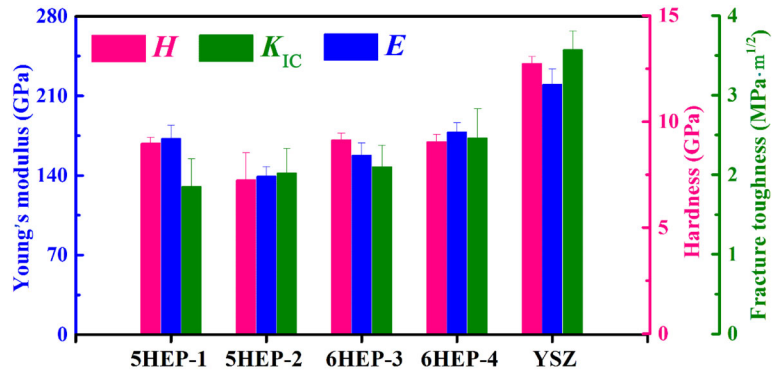
Fig. 3 Comparison of Young's modulus, hardness, and fracture toughness of (La$_{1/5}$Pr$_{1/5}$Dy$_{1/5}$Ho$_{1/5}$Tm$_{1/5}$)Ta$_3$O$_9$ (5HEP-1), (Gd$_{1/5}$Dy$_{1/5}$Ho$_{1/5}$Er$_{1/5}$Tm$_{1/5}$)Ta$_3$O$_9$ (5HEP-2), (La$_{1/6}$Sm$_{1/6}$Eu$_{1/6}$Dy$_{1/6}$Ho$_{1/6}$Tm$_{1/6}$)Ta$_3$O$_9$ (6HEP-3), (Eu$_{1/6}$Gd$_{1/6}$Dy$_{1/6}$Ho$_{1/6}$Er$_{1/6}$Tm$_{1/6}$)Ta$_3$O$_9$ (6HEP-4) ceramics, and YSZ.
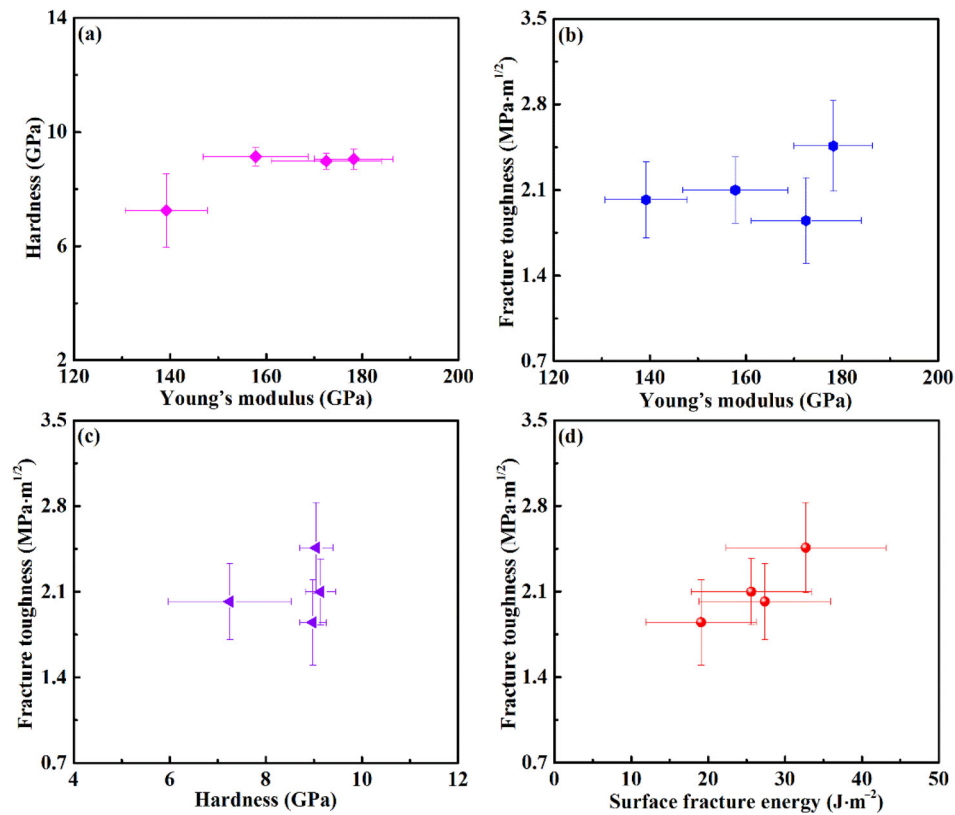
Fig. 4 Relationships among the mechanical properties of (La$_{1/5}$Pr$_{1/5}$Dy$_{1/5}$Ho$_{1/5}$Tm$_{1/5}$)Ta$_3$O$_9$ (5HEP-1), (Gd$_{1/5}$Dy$_{1/5}$Ho$_{1/5}$Er$_{1/5}$Tm$_{1/5}$)Ta$_3$O$_9$ (5HEP-2), (La$_{1/6}$Sm$_{1/6}$Eu$_{1/6}$Dy$_{1/6}$Ho$_{1/6}$Tm$_{1/6}$)Ta$_3$O$_9$ (6HEP-3), and (Eu$_{1/6}$Gd$_{1/6}$Dy$_{1/6}$Ho$_{1/6}$Er$_{1/6}$Tm$_{1/6}$)Ta$_3$O$_9$ (6HEP-4) ceramics: (a) hardness–Young's modulus, (b) fracture toughness–Young's modulus, (c) fracture toughness–hardness, and (d) fracture toughness–surface fracture energy.

0.57 are ductile [45]. Table 2 shows that the G/B ratio increases from 0.55 to 0.62, indicating that a brittle–ductile transition occurs with the difference in composition among the four HEP samples. The brittle–ductile transition is considered to increase the toughness. Small grains increase the hardness based on the Hall–Petch principle. The Young's modulus of the HEP samples are lower than those of the HECs of RE_3NbO_7 (210 GPa) [22] and $RE_2Zr_2O_7$ (240 GPa) [20], and close to those of the HECs of RE_2SiO_5 (170 GPa) [31] and ABO_3 (180 GPa) [17]. The relatively low Young's modulus of the HEP samples is attributed to their parent single-rare-earth $RETa_3O_9$ ceramics, where a comparatively low modulus promotes thermal stress reduction for high-temperature E/TBC applications [46].

3.4   Nanoindentation

The nano-Young's modulus (E_N = 140–180 GPa) and hardness (H_N = 10–11 GPa) are shown in Table 2 and Fig. 5. The slightly higher mean values measured by nanoindentation than those tested by normal methods (Fig. 5(a)) may be due to the indentation-size effect [47–49]. Figure 6 shows the 3D mapping of E_N and H_N, where there are slight variations over the testing area

because microstructure defects (pores and cracks) and test error can produce fluctuations in E_N and H_N. In Fig. 7, most of the nano-Young's modulus and hardness results are located around the mean values, and the hardness increases with the modulus. XRD patterns show that there are few precipitated $RETaO_4$ ceramics in the prepared samples, and SEM, EDS, and nanoindentation results jointly indicate the excellent compositional uniformity of the HEP $RETa_3O_9$. Furthermore, the differences in the Young's modulus of each sample tested by different methods in this study are less than 4%. The aforementioned results prove that the presence of a small quantity of precipitated $RETaO_4$ ceramics does not affect the Young's modulus, hardness, and toughness of the HEP $RETa_3O_9$. Normally, increases in the Young's modulus and acoustic velocity reflect increases in the phonon propagation speed and thermal conductivity, which is discussed in Section 3.5 Thermal properties.

The results of the advanced dynamic E and H tests using nanoindentation are shown in Figs. 5(b)–5(f), where the investigated parameters include the hardness, Young's modulus, indentation depth, and load. The indentation depth is proportional to the load, which has a maximum value of 100 mN in the current study. The H_N and E_N values for indentation depths less than 100 nm
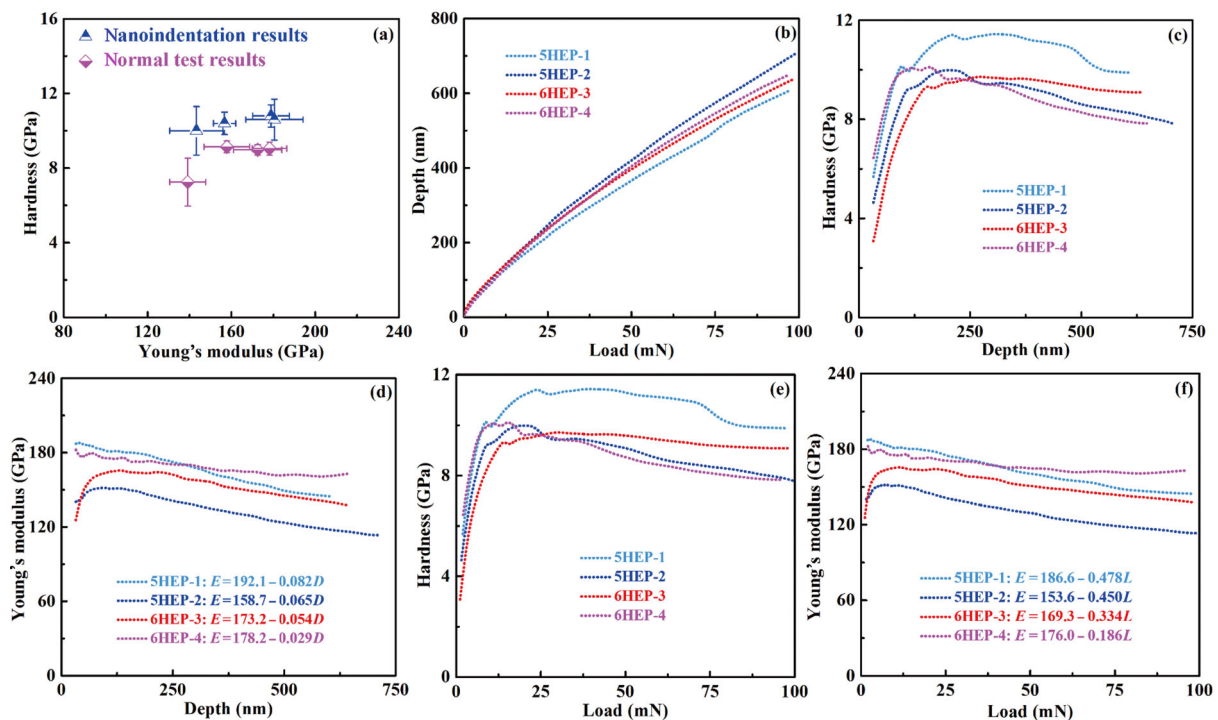

Fig. 5   Mechanical properties of $(La_{1/5}Pr_{1/5}Dy_{1/5}Ho_{1/5}Tm_{1/5})Ta_3O_9$ (5HEP-1), $(Gd_{1/5}Dy_{1/5}Ho_{1/5}Er_{1/5}Tm_{1/5})Ta_3O_9$ (5HEP-2), $(La_{1/6}Sm_{1/6}Eu_{1/6}Dy_{1/6}Ho_{1/6}Tm_{1/6})Ta_3O_9$ (6HEP-3), and $(Eu_{1/6}Gd_{1/6}Dy_{1/6}Ho_{1/6}Er_{1/6}Tm_{1/6})Ta_3O_9$ (6HEP-4) ceramics: (a) nano-Young's modulus and hardness measured by different methods, (b–f) variations in different parameters observed during nanoindentation advanced dynamic E and H tests.
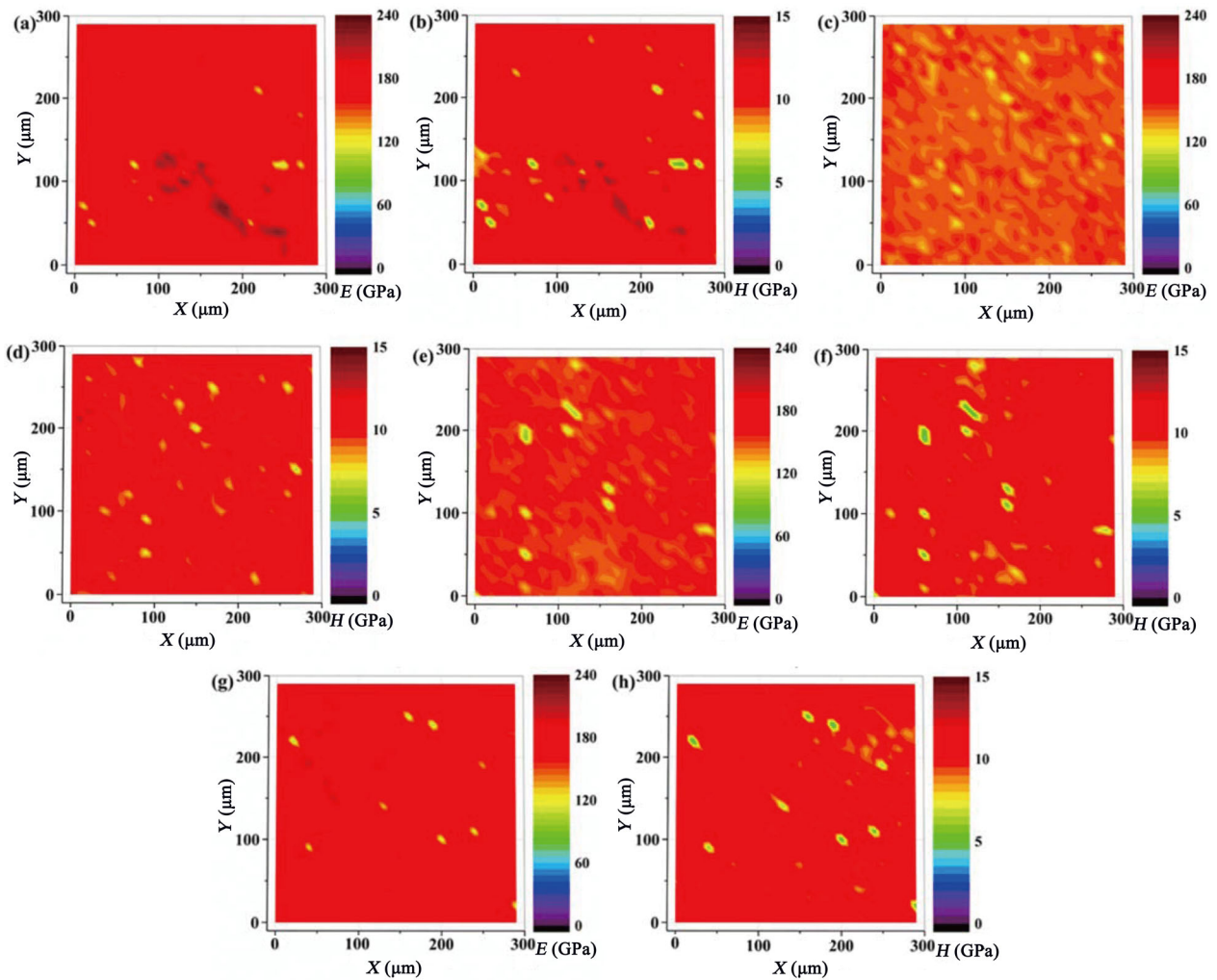
Fig. 6 3D mapping of Young's modulus (E) and hardness (H) for HEP RETa$_3$O$_9$ ceramics: (a, b) (La$_{1/5}$Pr$_{1/5}$Dy$_{1/5}$Ho$_{1/5}$Tm$_{1/5}$)Ta$_3$O$_9$ (5HEP-1), (c, d) (Gd$_{1/5}$Dy$_{1/5}$Ho$_{1/5}$Er$_{1/5}$Tm$_{1/5}$)Ta$_3$O$_9$ (5HEP-2), (e, f) (La$_{1/6}$Sm$_{1/6}$Eu$_{1/6}$Dy$_{1/6}$Ho$_{1/6}$Tm$_{1/6}$)Ta$_3$O$_9$ (6HEP-3), and (g, h) (Eu$_{1/6}$Gd$_{1/6}$Dy$_{1/6}$Ho$_{1/6}$Er$_{1/6}$Tm$_{1/6}$)Ta$_3$O$_9$ (6HEP-4).

are not considered here because the indenter appearance is not self-similar, and the contact area is indeterminate at small indentation depths (low indentation loads) [47]. H_N and E_N decrease as the depth and load increase, for test depths beyond 100 nm or loads heavier than 15 mN. During the nanoindentation continuous stiffness test (using the advanced dynamic E and H model), the decrease in the strain gradient results in weakened hardening as the indentation depth and load increase [48–52]. In addition to the strain gradient, other factors affect the hardness and modulus of some materials. The grain size (the grain boundary density), pore, crack, and surface roughness may affect the hardness, toughness, and modulus. Considering the relative density and purity of the HEP RETa$_3$O$_9$, macro-defects should have little effect on the hardness and modulus, that is,

the strain gradient is the predominant factor. The relationships between the Young's modulus and depth/load are shown in Figs. 5(d) and 5(f), respectively, and their slopes indicate the decreasing rate of the strain gradient in conjunction with increments of load/depth. In addition to the surface micro-defects, the internal micro-defect density affects the modulus and toughness of the prepared ceramics. The results of the advanced dynamic E and H tests show that the internal micro-defect density of the HEP RETa$_3$O$_9$ decreases in the order of 5HEP-1 > 5HEP-2 > 6HEP-3 > 6HEP-4, based on the decrease in the modulus with increasing depth.

3.5 Thermal properties

Figure 8(a) indicates that the thermal diffusivity of the HEP RETa$_3$O$_9$ samples initially decreases with the

increase of temperature, and then clearly increases at high temperatures ($\geqslant$ 500 ℃). Figure 8(b) shows that the thermal conductivity of the HEP RETa$_3$O$_9$ exhibits a similar temperature dependence to that of the corresponding single-rare-earth samples, which is caused by a high concentration of A-site cation vacancies and

thermal radiation [15,53]. Increases in thermal conductivity caused by thermal radiation have been reported for YSZ [34], La$_2$Zr$_2$O$_7$ [54], RETaO$_4$ [42], RE$_2$SiO$_5$ [31], and ABO$_3$ perovskite ceramics [17]. Evidently, the prepared samples have lower thermal conductivity than those of SrZrO$_3$ [55], YSZ [44], and many
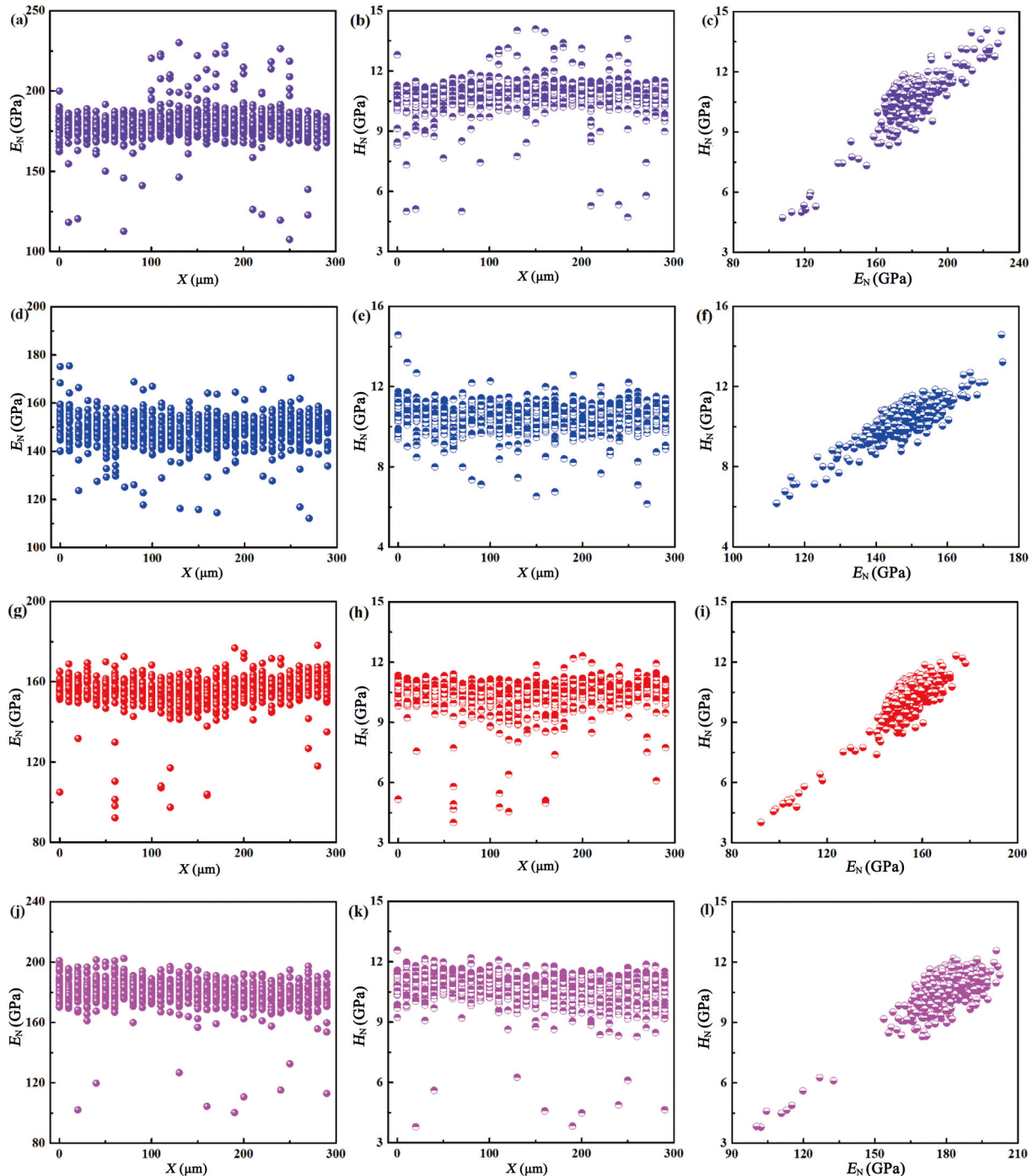

Fig. 7 Distributions of numerical values of nano-Young's modulus and hardness for HEP RETa$_3$O$_9$ ceramics: (a–c) (La$_{1/5}$Pr$_{1/5}$Dy$_{1/5}$Ho$_{1/5}$Tm$_{1/5}$)Ta$_3$O$_9$ (5HEP-1), (d–f) (Gd$_{1/5}$Dy$_{1/5}$Ho$_{1/5}$Er$_{1/5}$Tm$_{1/5}$)Ta$_3$O$_9$ (5HEP-2), (g–i) (La$_{1/6}$Sm$_{1/6}$Eu$_{1/6}$Dy$_{1/6}$Ho$_{1/6}$Tm$_{1/6}$)Ta$_3$O$_9$ (6HEP-3), and (j–l) (Eu$_{1/6}$Gd$_{1/6}$Dy$_{1/6}$Ho$_{1/6}$Er$_{1/6}$Tm$_{1/6}$)Ta$_3$O$_9$ (6HEP-4).
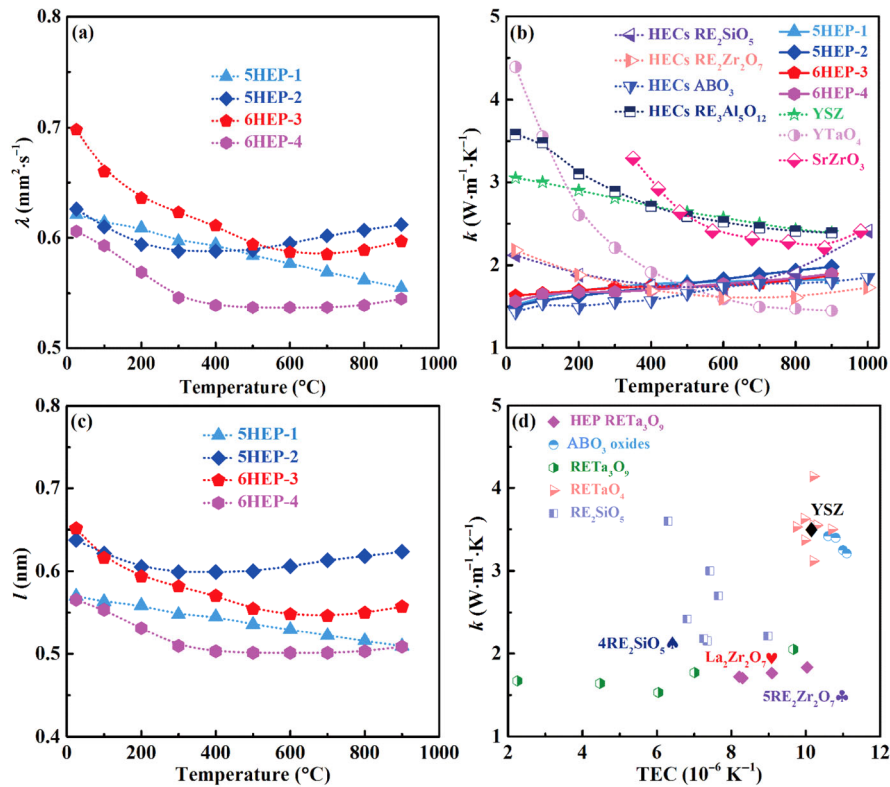
Fig. 8 Thermal properties of $(La_{1/5}Pr_{1/5}Dy_{1/5}Ho_{1/5}Tm_{1/5})Ta_3O_9$ (5HEP-1), $(Gd_{1/5}Dy_{1/5}Ho_{1/5}Er_{1/5}Tm_{1/5})Ta_3O_9$ (5HEP-2), $(La_{1/6}Sm_{1/6}Eu_{1/6}Dy_{1/6}Ho_{1/6}Tm_{1/6})Ta_3O_9$ (6HEP-3), and $(Eu_{1/6}Gd_{1/6}Dy_{1/6}Ho_{1/6}Er_{1/6}Tm_{1/6})Ta_3O_9$ (6HEP-4) ceramics: (a) thermal diffusivity, (b) thermal conductivity, (c) phonon mean free path, and (d) thermal properties compared with other oxides in Refs. [6,10,14,15,17,23,42,44,53–58].

other oxides [57,58]. Note that HEP $RETa_3O_9$ and HECs ABO_3 $(Zn_{0.1}Ca_{0.1}Sr_{0.4}Ba_{0.4}ZrO_3)$ [17] exhibit similar thermal conductivity, which implies that amorphous-like thermal conductivity may be a common feature of HEP oxides. Furthermore, the thermal conductivity of the HEP samples is lower than those of HECs of RE_2SiO_5 [31] and $RE_3Al_5O_{12}$ [30], and close to those of HECs of $RE_2Zr_2O_7$ [20]. The lower the thermal conductivity of an HEP sample, the higher the thermal insulation performance is. The temperature dependence of the phonon mean free path (*l*) shown in Fig. 8(c) is similar to that of the thermal diffusivity, which further suggests the presence of thermal radiation. Figure 8(d) shows that the TECs range from 8.0×10^{-6} to 10.1×10^{-6} K^{-1} (1473 K), which exceeds those of $GdTa_3O_9$ $(3.6 \times 10^{-6}$ K$^{-1})$, $SmTa_3O_9$ $(5.0 \times 10^{-6}$ K$^{-1})$, and $DyTa_3O_9$ $(7.5 \times 10^{-6}$ K$^{-1})$, and lattice relaxation may be the predominant factor in the enhanced thermal expansion of the HEP samples [15]. The enhanced TECs of the HEP $RETa_3O_9$ can expand applications of these materials, e.g., as EBCs on the surface of Al_2O_3 fibre-enhanced Al_2O_3 ceramic matrix composites $(Al_2O_{3f}/Al_2O_3$ with TECs of 8.5×10^{-6}– 9.0×10^{-6} K$^{-1})$

because of matched TECs [10]. In addition, no phase transition is detected during the TECs test up to 1200 ℃, which demonstrates the extraordinarily high-temperature phase stability of the prepared HEP $RETa_3O_9$ ceramics. Obviously, the TECs of the $RETa_3O_9$ are successfully regulated in the fabricated HECs, which exhibit outstanding phase stability.

Figure 8(d) shows that the HEP $RETa_3O_9$ oxides have higher TECs compared with those of RE_2SiO_5 $(6.3 \times 10^{-6}$–9.0×10^{-6} K$^{-1})$ [58] and $La_2Zr_2O_7$ $(9.0 \times 10^{-6}$ K$^{-1})$ [6] and lower thermal conductivity compared with various E/TBCs [6,10,14,15,17,23,42,44,53–58]. HECs typically have lower thermal conductivity compared with their parent ceramics; however, this trend is not borne out for HEP $RETa_3O_9$. The point defect phonon scattering principle is not applicable for analysing the thermal transport properties of the prepared samples because of (1) the formation of random solid solutions, (2) severe lattice distortion, and (3) the cocktail effect of HECs [59,60]. As the *E*/*k* ratio reflects the phonon scattering rate, an increase in *E*/*k* causes a decrease in the thermal conductivity. The *E*/*k* ratio is 113.8, 92.6, 96.9, and 114.1 GPa·W^{-1}·m·K for 5HEP-1 (*k*:

1.52 W·m^{-1}·K^{-1}), 5HEP-2 (*k*: 1.50 W·m^{-1}·K^{-1}), 6HEP-3 (*k*: 1.63 W·m^{-1}·K^{-1}), and 6HEP-4 (*k*: 1.56 W·m^{-1}·K^{-1}), respectively. Herein, the prominent differences in the Young's modulus, *E*/*k* ratio, and acoustic velocity among the four HEP ceramics do not noticeably affect the thermal conductivity. Grain refinements are found in the prepared samples: Fig. 2 shows that most grains are micron-sized and are therefore considerably larger than the nanoscale phonon mean free path. Herein, the phonon scattering strength from the grain boundary is not taken into account. The increasing degree of lattice distortion may decrease the thermal conductivity of perovskites, where the distortion degree is reflected by the tolerance factor (*t*). In the HEP RETa$_3$O$_9$, fluctuations in the disorder parameters for the electronegativity (δ_A^e), ionic radius (δ_A^r), and atomic mass (δ_A^m) in the A-site sublattice may change the thermal conductivity [17,61,62]:

$$\delta_A^e = \sqrt{\sum_i c_i \left(1 - \frac{e_A^i}{\overline{e_A}}\right)^2} \tag{11}$$

$$\delta_A^r = \sqrt{\sum_i c_i \left(1 - \frac{r_A^i}{\overline{r_A}}\right)^2} \tag{12}$$

$$\delta_A^m = \sqrt{\sum_i c_i \left(1 - \frac{m_A^i}{\overline{m_A}}\right)^2} \tag{13}$$

where c_i denotes the atomic ratio of the ith RE element; e_A^i denotes the electronegativity of the ith RE element, and $\overline{e_A}$ denotes the mean electronegativity of an A-site atom; r_A^i denotes the ionic radius of the ith RE element, and $\overline{r_A}$ denotes the mean ionic radius of an A-site atom; m_A^i denotes the atomic mass of the ith RE element, and $\overline{m_A}$ indicates the mean atomic mass of an A-site atom. Table 3 displays the values of the aforementioned parameters. The variation trends in the thermal conductivity with *t*, δ_A^e, δ_A^r, and δ_A^m are shown in Fig. 9. No regular variation trends are found

Table 3 Effective RE^{3+} ionic radius at the A-site (r_A), tolerance factor (*t*), electronegativity disorder parameter (δ_A^e), ionic radius disorder parameter (δ_A^r), and atomic mass disorder parameter (δ_A^m) of HEP RETa$_3$O$_9$ ceramics

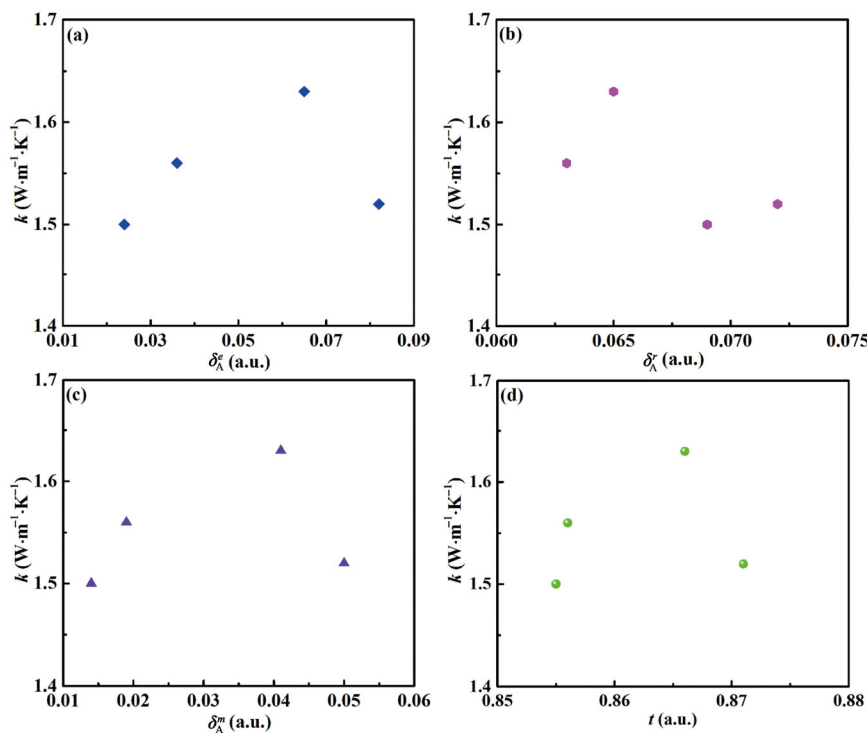| Sample	r_A (nm)	t	δ_A^e	δ_A^r	δ_A^m
5HEP-1	0.109	0.871	0.082	0.072	0.050
5HEP-2	0.105	0.855	0.024	0.069	0.014
6HEP-3	0.108	0.866	0.065	0.065	0.041
6HEP-4	0.105	0.856	0.036	0.063	0.019

Fig. 9 Variation trends in thermal conductivity with different parameters of (La$_{1/5}$Pr$_{1/5}$Dy$_{1/5}$Ho$_{1/5}$Tm$_{1/5}$)Ta$_3$O$_9$ (5HEP-1), (Gd$_{1/5}$Dy$_{1/5}$Ho$_{1/5}$Er$_{1/5}$Tm$_{1/5}$)Ta$_3$O$_9$ (5HEP-2), (La$_{1/6}$Sm$_{1/6}$Eu$_{1/6}$Dy$_{1/6}$Ho$_{1/6}$Tm$_{1/6}$)Ta$_3$O$_9$ (6HEP-3), and (Eu$_{1/6}$Gd$_{1/6}$Dy$_{1/6}$Ho$_{1/6}$Er$_{1/6}$Tm$_{1/6}$)Ta$_3$O$_9$ (6HEP-4) ceramics: A-site atomic disorder parameters of (a) electronegativity, (b) ionic radius, and (c) atomic mass; (d) tolerance factor.

for the thermal conductivity with the aforementioned four parameters; thus, more HEP specimens should be fabricated and tested to identify variation laws. The four investigated samples clearly exhibit low thermal conductivity and high TECs, and they are therefore candidate E/TBCs.

4   Conclusions

Four novel A-site equiatomic HEP $RETa_3O_9$ ceramics are fabricated via a two-step sintering process, and the corresponding thermophysical properties are investigated and analysed as candidate E/TBCs for high-temperature applications. The contributions of this study are presented below:

1) Dense and high-purity HEP $RETa_3O_9$ bulk ceramics are successfully fabricated via SPS, and XRD, SEM, EDS, and 3D nanoindentation results demonstrate the excellent compositional homogeneity of all the samples.

2) The tolerance factor of the prepared HEP samples depends on the ionic radius of RE^{3+}, where the tolerance factor ranging from 0.8 to 0.9 shows that the samples have stable double-perovskite structures.

3) HEP $RETa_3O_9$ has a moderate Young's modulus (140–180 GPa) and hardness (7–10 GPa), and the brittle–ductile transition results in increased toughness (1.8–2.5 MPa·m$^{1/2}$).

4) Enhanced TECs (8.0×10^{-6}–10.1×10^{-6} K^{-1} at 1473 K) expand the applications of $RETa_3O_9$, and a high melting point and extraordinary phase stability ensure high-temperature applications.

5) A low thermal conductivity (1.5–2.0 W·m^{-1}·K^{-1}) indicates excellent thermal insulation by HEP $RETa_3O_9$ ceramics, and the results of this study have inspired a future study on tantalate HECs with desirable properties.

Acknowledgements

References

[1]   Shian S, Sarin P, Gurak M, *et al*. The tetragonal–monoclinic, ferroelastic transformation in yttrium tantalate and effect of zirconia alloying. *Acta Mater* 2014, **69**: 196–202.

[2]   Song WJ, Lavallée Y, Hess KU, *et al*. Volcanic ash melting under conditions relevant to ash turbine interactions. *Nat Commun* 2016, **7**: 10795.

[3]   Li F, Zhou L, Liu JX, *et al*. High-entropy pyrochlores with low thermal conductivity for thermal barrier coating materials. *J Adv Ceram* 2019, **8**: 576–582.

[4]   Feng J, Shian S, Xiao B, *et al*. First-principles calculations of the high-temperature phase transformation in yttrium tantalate. *Phys Rev B* 2014, **90**: 094102.

[5]   Xiang HM, Xing Y, Dai FZ, *et al*. High-entropy ceramics: Present status, challenges, and a look forward. *J Adv Ceram* 2021, **10**: 385–441.

[6]   Liu B, Liu YC, Zhu CH, *et al*. Advances on strategies for searching for next generation thermal barrier coating materials. *J Mater Sci Technol* 2019, **35**: 833–851.

[7]   Chen L, Yang GJ. Epitaxial growth and cracking of highly tough 7YSZ splats by thermal spray technology. *J Adv Ceram* 2018, **7**: 17–29.

[8]   Chen L, Feng J. Influence of HfO_2 alloying effect on microstructure and thermal conductivity of $HoTaO_4$ ceramics. *J Adv Ceram* 2019, **8**: 537–544.

[9]   Liu MJ, Zhang G, Lu YH, *et al*. Plasma spray–physical vapor deposition toward advanced thermal barrier coatings: A review. *Rare Met* 2020, **39**: 479–497.

[10]   Sun YN, Xiang HM, Dai FZ, *et al*. Preparation and properties of CMAS resistant bixbyite structured high-entropy oxides RE_2O_3 (RE = Sm, Eu, Er, Lu, Y, and Yb): Promising environmental barrier coating materials for Al_2O_{3f}/Al_2O_3 composites. *J Adv Ceram* 2021, **10**: 596–613.

[11]   Garcia E, Lee H, Sampath S. Phase and microstructure evolution in plasma sprayed $Yb_2Si_2O_7$ coatings. *J Eur Ceram Soc* 2019, **39**: 1477–1486.

[12]   Kakisawa H, Nishimura T. A method for testing the interface toughness of ceramic environmental barrier coatings (EBCs) on ceramic matrix composites (CMCs). *J Eur Ceram Soc* 2018, **38**: 655–663.

[13]   Zhou YX, Zhou Y, Wu P, *et al*. Thermal properties of $Y_{1-x}Mg_xTaO_{4-x/2}$ ceramics via anion sublattice adjustment. *Rare Met* 2020, **39**: 545–554.

[14]   Chen L, Song P, Feng J. Influence of ZrO_2 alloying effect on the thermophysical properties of fluorite-type Eu_3TaO_7 ceramics. *Scripta Mater* 2018, **152**: 117–121.

[15]   Chen L, Jiang YH, Chong XY, *et al*. Synthesis and thermophysical properties of $RETa_3O_9$ (RE = Ce, Nd, Sm, Eu, Gd, Dy, Er) as promising thermal barrier coatings. *J Am Ceram Soc* 2018, **101**: 1266–1278.

[16]   Zhao ZF, Chen H, Xiang HM, *et al*. High entropy defective fluorite structured rare-earth niobates and tantalates for thermal barrier applications. *J Adv Ceram* 2020, **9**: 303–311.

[17]   Liu YC, Jia DC, Zhou Y, *et al*. $Zn_{0.1}Ca_{0.1}Sr_{0.4}Ba_{0.4}ZrO_3$: A

non-equimolar multicomponent perovskite ceramic with low thermal conductivity. *J Eur Ceram Soc* 2020, **40**: 6272–6277.

[18] Ogawa T, Matsudaira T, Yokoe D, *et al*. Spontaneously formed nanostructures in double perovskite rare-earth tantalates for thermal barrier coatings. *Acta Mater* 2021, **216**: 117152.

[19] Ye BL, Wen TQ, Nguyen MC, *et al*. First-principles study, fabrication and characterization of $(Zr_{0.25}Nb_{0.25}Ti_{0.25}V_{0.25})C$ high-entropy ceramics. *Acta Mater* 2019, **170**: 15–23.

[20] Wright AJ, Wang QY, Huang CY, *et al*. From high-entropy ceramics to compositionally-complex ceramics: A case study of fluorite oxides. *J Eur Ceram Soc* 2020, **40**: 2120–2129.

[21] Sun LC, Luo YX, Tian ZL, *et al*. High temperature corrosion of $(Er_{0.25}Tm_{0.25}Yb_{0.25}Lu_{0.25})_2Si_2O_7$ environmental barrier coating material subjected to water vapor and molten calcium–magnesium–aluminosilicate (CMAS). *Corros Sci* 2020, **175**: 108881.

[22] Chen L, Wang YT, Hu MY, *et al*. Achieved limit thermal conductivity and enhancements of mechanical properties in fluorite RE_3NbO_7 via entropy engineering. *Appl Phys Lett* 2021, **118**: 071905.

[23] Ren K, Wang QK, Shao G, *et al*. Multicomponent high-entropy zirconates with comprehensive properties for advanced thermal barrier coating. *Scripta Mater* 2020, **178**: 382–386.

[24] Sarkar A, Wang QS, Schiele A, *et al*. High-entropy oxides: Fundamental aspects and electrochemical properties. *Adv Mater* 2019, **31**: 1806236.

[25] Ye YF, Wang Q, Lu J, *et al*. High-entropy alloy: Challenges and prospects. *Mater Today* 2016, **19**: 349–362.

[26] Cantor B, Chang ITH, Knight P, *et al*. Microstructural development in equiatomic multicomponent alloys. *Mater Sci Eng A* 2004, **375–377**: 213–218.

[27] Liu B, Zhao JL, Liu YC, *et al*. Application of high-throughput first-principles calculations in ceramic innovation. *J Mater Sci Technol* 2021, **88**: 143–157.

[28] Qin Y, Liu JX, Li F, *et al*. A high entropy silicide by reactive spark plasma sintering. *J Adv Ceram* 2019, **8**: 148–152.

[29] Oses C, Toher C, Curtarolo S. High-entropy ceramics. *Nat Rev Mater* 2020, **5**: 295–309.

[30] Chen H, Zhao ZF, Xiang HM, *et al*. High entropy $(Y_{0.2}Yb_{0.2}Lu_{0.2}Eu_{0.2}Er_{0.2})_3Al_5O_{12}$: A novel high temperature stable thermal barrier material. *J Mater Sci Technol* 2020, **48**: 57–62.

[31] Ren XM, Tian ZL, Zhang J, *et al*. Equiatomic quaternary $(Y_{1/4}Ho_{1/4}Er_{1/4}Yb_{1/4})_2SiO_5$ silicate: A perspective multifunctional thermal and environmental barrier coating material. *Scripta Mater* 2019, **168**: 47–50.

[32] Ramadass N. ABO_3-type oxides—Their structure and properties—A bird's eye view. *Mater Sci Eng* 1978, **36**: 231–239.

[33] Jiang SC, Hu T, Gild J, *et al*. A new class of high-entropy perovskite oxides. *Scripta Mater* 2018, **142**: 116–120.

[34] Stanek CR, McClellan KJ, Levy MR, *et al*. Defect behavior in rare earth $REAlO_3$ scintillators. *J Appl Phys* 2006, **99**: 113518.

[35] Bai H, Li J, Hong Y, *et al*. Enhanced ferroelectricity and magnetism of quenched $(1−x)BiFeO_3–xBaTiO_3$ ceramics. *J Adv Ceram* 2020, **9**: 511–516.

[36] Lim H, Lim J, Jang S, *et al*. Emissions of Er^{3+} and Yb^{3+} co-doped $SrZrO_3$ nanocrystals under near-infrared and near-ultraviolet excitations. *J Adv Ceram* 2020, **9**: 413–423.

[37] Chantikul P, Anstis GR, Lawn BR, *et al*. A critical evaluation of indentation techniques for measuring fracture toughness: II, strength method. *J Am Ceram Soc* 1981, **64**: 539–543.

[38] Anstis GR, Chantikul P, Lawn BR, *et al*. A critical evaluation of indentation techniques for measuring fracture toughness: I, direct crack measurements. *J Am Ceram Soc* 1981, **64**: 533–538.

[39] Sanditov DS, Belomestnykh VN. Relation between the parameters of the elasticity theory and averaged bulk modulus of solids. *Tech Phys* 2011, **56**: 1619–1623.

[40] Schlichting KW, Padture NP, Klemens PG. Thermal conductivity of dense and porous yttria-stabilized zirconia. *J Mater Sci* 2001, **36**: 3003–3010.

[41] Kittel C. Introduction to solid state physics. *Phys Today* 1957, **10**: 43–44.

[42] Chen L, Hu MY, Wu P, *et al*. Thermal expansion performance and intrinsic lattice thermal conductivity of ferroelastic $RETaO_4$ ceramics. *J Am Ceram Soc* 2019, **102**: 4809–4821.

[43] Flamant Q, Gurak M, Clarke DR. The effect of zirconia substitution on the high-temperature transformation of the monoclinic-prime phase in yttrium tantalate. *J Eur Ceram Soc* 2018, **38**: 3925–3931.

[44] Zhao M, Ren XR, Yang J, *et al*. Thermo-mechanical properties of ThO_2-doped Y_2O_3 stabilized ZrO_2 for thermal barrier coatings. *Ceram Int* 2016, **42**: 501–508.

[45] Pugh SF. XCII. Relations between the elastic moduli and the plastic properties of polycrystalline pure metals. *Lond Edinb Dublin Philos Mag J Sci* 1954, **45**: 823–843.

[46] Kingery WD. Factors affecting thermal stress resistance of ceramic materials. *J Am Ceram Soc* 1955, **38**: 3–15.

[47] Nix WD, Gao HJ. Indentation size effects in crystalline materials: A law for strain gradient plasticity. *J Mech Phys Solids* 1998, **46**: 411–425.

[48] Li XD, Bhushan B. A review of nanoindentation continuous stiffness measurement technique and its applications. *Mater Charact* 2002, **48**: 11–36.

[49] Gong JH, Deng B, Jiang DY. On the efficiency of the "effective truncation length" of indenter tip in mechanical property determination with nanoindentation tests. *Mater Today Commun* 2020, **25**: 101412.

[50] Shell De Guzman M, Neubauer G, Flinn P, *et al*. The role of

indentation depth on the measured hardness of materials. *MRS Proc* 1993, **308**: 613.

[51] Gong JH, Deng B, Qiu HP, *et al*. Description of the nanoindentation unloading curves with a universal function: Theoretical consideration and applications to brittle materials. *Mater Chem Phys* 2020, **251**: 123165.

[52] Li JY, Dai H, Zhong XH, *et al*. Lanthanum zirconate ceramic toughened by BaTiO$_3$ secondary phase. *J Alloys Compd* 2008, **452**: 406–409.

[53] Popuri SR, Scott AJM, Downie RA, *et al*. Glass-like thermal conductivity in SrTiO$_3$ thermoelectrics induced by A-site vacancies. *RSC Adv* 2014, **4**: 33720–33723.

[54] Yang J, Wan CL, Zhao M, *et al*. Effective blocking of radiative thermal conductivity in La$_2$Zr$_2$O$_7$/LaPO$_4$ composites for high temperature thermal insulation applications. *J Eur Ceram Soc* 2016, **36**: 3809–3814.

[55] Ma W, Mack DE, Vaßen R, *et al*. Perovskite-type strontium zirconate as a new material for thermal barrier coatings. *J Am Ceram Soc* 2008, **91**: 2630–2635.

[56] Chen L, Wu P, Song P, *et al*. Potential thermal barrier coating materials: RE$_3$NbO$_7$ (RE = La, Nd, Sm, Eu, Gd, Dy) ceramics. *J Am Ceram Soc* 2018, **101**: 4503–4508.

[57] Li GR, Lei J, Yang GJ, *et al*. Substrate-constrained effect on the stiffening behavior of lamellar thermal barrier coatings. *J Eur Ceram Soc* 2018, **38**: 2579–2587.

[58] Tian ZL, Zhang J, Zhang TY, *et al*. Towards thermal barrier coating application for rare earth silicates RE$_2$SiO$_5$ (RE = La, Nd, Sm, Eu, and Gd). *J Eur Ceram Soc* 2019, **39**: 1463–1476.

[59] Yeh JW. Recent progress in high-entropy alloys. *Eur J Control* 2006, **31**: 633–648.

[60] Ranganathan S. Alloyed pleasures: Multimetallic cocktails. *Curr Sci* 2003, **85**: 1404–1406.

[61] Wright AJ, Wang QY, Ko ST, *et al*. Size disorder as a descriptor for predicting reduced thermal conductivity in medium-and high-entropy pyrochlore oxides. *Scripta Mater* 2020, **181**: 76–81.

[62] Garg J, Bonini N, Kozinsky B, *et al*. Role of disorder and anharmonicity in the thermal conductivity of silicon–germanium alloys: A first-principles study. *Phys Rev Lett* 2011, **106**: 045901.